# Estimation of $\pi-\pi$ Electronic Couplings from Current Measurements

J. Trasobares,[†,#] J. Rech,[‡,#] T. Jonckheere,[‡] T. Martin,[‡] O. Aleveque,[§] E. Levillain,[§] V. Diez-Cabanes,[∥]
Y. Olivier,[∥] J. Cornil,[∥] J. P. Nys,[†] R. Sivakumarasamy,[†] K. Smaali,[†] P. Leclere,[∥] A. Fujiwara,[⊥] D. Théron,[†]
D. Vuillaume,[†] and N. Clément[*,†,⊥]

[†]Institute of Electronics, Microelectronics and Nanotechnology, CNRS, University of Lille, Avenue Poincaré, BP60069, 59652, Villeneuve d'Ascq France

[‡]Aix Marseille University, Universite de Toulon, CNRS, CPT, 163 Avenue de Luminy, 13288 Marseille cedex 9, France

[§]Université d'Angers, CNRS UMR 6200, Laboratoire MOLTECH-Anjou, 2 bd Lavoisier, 49045 Angers cedex, France

[∥]Laboratory for Chemistry of Novel Materials, University of Mons, Place du Parc 20, B-7000 Mons, Belgium

[⊥]NTT Basic Research Laboratories, 3-1, Morinosato Wakamiya, Atsugi-shi, kanagawa 243-0198, Japan

S *Supporting Information*

ABSTRACT: The $\pi-\pi$ interactions between organic molecules are among the most important parameters for optimizing the transport and optical properties of organic transistors, light-emitting diodes, and (bio-) molecular devices. Despite substantial theoretical progress, direct experimental measurement of the $\pi-\pi$ electronic coupling energy parameter t has remained an old challenge due to molecular structural variability and the large number of parameters that affect the charge transport. Here, we propose a study of $\pi-\pi$ interactions from electrochemical and current measurements on a large array of ferrocene-thiolated gold nanocrystals. We confirm the theoretical prediction that t can be assessed from a statistical analysis of current histograms. The extracted value of $t \approx 35$ meV is in the expected range based on our density functional theory analysis. Furthermore, the t distribution is not necessarily Gaussian and could be used as an ultrasensitive technique to assess intermolecular distance fluctuation at the subangström level. The present work establishes a direct bridge between quantum chemistry, electrochemistry, organic electronics, and mesoscopic physics, all of which were used to discuss results and perspectives in a quantitative manner.

KEYWORDS: *Cooperative effect, $\pi-\pi$ interaction, transfer integral, molecular electronics, nanoelectrochemistry, coupled quantum dot*
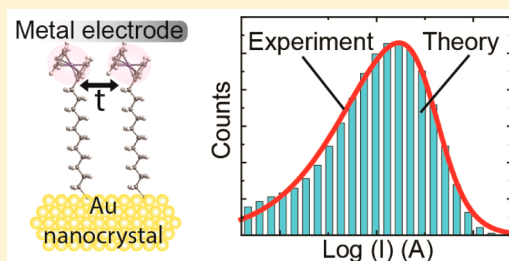
Interactions between π-systems[1,2] are involved in diverse and important phenomena, such as the stabilization of the double helical structure of DNA,[3] protein folding,[4] molecular recognition,[5] drug design,[6] and crystal engineering.[7] These interactions are of fundamental technological importance for the development of organic-based devices,[8] in particular for organic light-emitting diodes,[9] field-effect transistors,[10] or (bio-) molecular devices.[11−16] A key parameter in these interactions is the transfer integral (or electronic coupling energy) parameter t, which is included as t^2 in simple semiclassical formulations of charge carrier mobility.[17] In symmetric dimers, t is directly related to energy-level splitting of the highest occupied/lowest unoccupied molecular orbital (HOMO/LUMO) due to intermolecular interactions for hole and electron transport, respectively.[8]

The parameter t has mainly been discussed by using photoelectron spectroscopy and quantum-chemical calculations.[18−20] In the ideal scenario for (opto-)electronic applications, t should be deduced directly from electronic measurements in a device configuration and related to the molecular structure. Such knowledge of t would help us to understand and optimize charge transport through molecular

systems. For example, cooperative effects, induced by molecule−molecule and molecule/electrode electronic couplings, are attracting substantial theoretical attention.[21,22] The distribution or fluctuation of t plays a key role in the charge transport through organic semiconductors or biomolecules by inducing charge localization or conformational gating effects.[23−25] A Gaussian distribution of t with a standard deviation (SD) in the range of the mean t is usually assumed from thermal molecular motions[25] but remains to be confirmed experimentally. The experimental measurement of t could potentially be used as an ultrasensitive chemical characterization technique because t is expected to be more sensitive to molecular structural order than other physical constants such as $\pi-\pi$ electrostatic interactions (φ) measured by cyclic voltammetry (CV) (Figure 1a). However, recent efforts to establish correlations between electrochemical and molecular electronics results[26−31] have neglected $\pi-\pi$ intermolecular interactions.
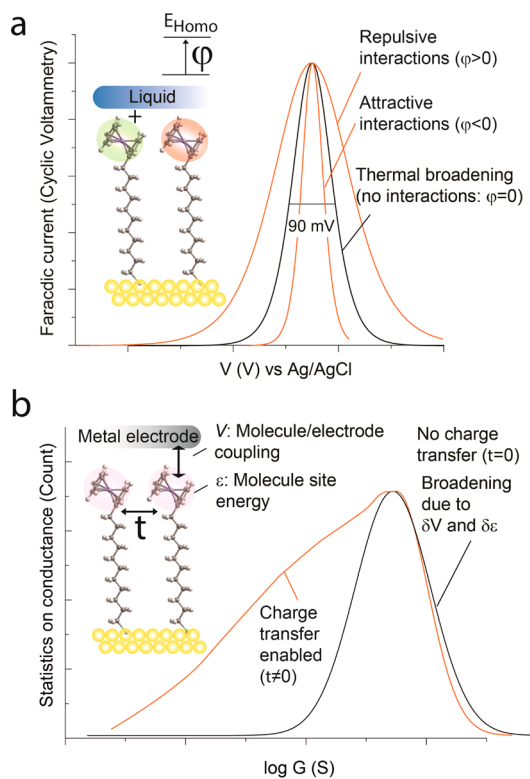
Figure 1. Signatures of cooperative effects with the introduction of parameters φ and t. (a) Schematic representation of CV results in the absence (black curve) and presence (orange curves) of Coulomb interactions between Fc molecules according to the Laviron model[27] based on the Frumkin isotherm. Inset: Schematic representation of the microscopic process. When Fc is oxidized (green cloud), it shifts the energy level of the neighboring molecule by φ. (b) Schematic representation of a theoretically predicted[21] conductance histogram in the absence (black curve) and presence (orange curve) of coupling between two molecules (tight binding model). Inset: Schematic representation of intermolecular coupling (t) related to charge transfer between adjacent molecules.

To reach these goals, two main issues need to be addressed. A first issue is related to disorder. Structural variability makes it difficult to extract t from electronic measurements because t is extremely sensitive to order at the angstrom level.[8] One recently implemented and elegant way to measure charge transport at the local scale is through photoinduced time-resolved microwave conductivity (TRMC),[32] but this contactless approach differs from the measurement of charge transport in a device configuration. The alternative approach is to reduce electrodes and organic layer dimensions.

A second issue is that comparisons between experimental and theoretical charge transport data are usually qualitative. Even without molecular organization disorder, many parameters influence the measured current including molecule/molecule or molecule/electrode coupling and electron-vibration (phonon) interactions.[8,33] A recent theoretical proposal suggested additional degrees of freedom. Reuter et al. found that quantitative information on cooperative effects may be assessed by statistical analysis of conductance traces.[21,34] This approach is based on the Landauer Buttiker Imry formalism that typically is used in mesoscopic physics for the study of electron transport through quantum dots in the coherent regime. The related experimental model system is a single layer of π-conjugated molecules (quantum dots), which

is sandwiched between two electrodes. Thousands of molecular junctions are required for statistical analysis. The authors suggested that cooperative effects between molecules should provide asymmetrical conductance histogram spectra (Figure 1b). Histogram fitting may be achieved by considering the mean and SD of molecule site energies (ε, $\delta\varepsilon$), molecule-electrode coupling (V, δV) and transfer integrals ($\langle t \rangle$, δt).[21] This fitting differs from the usual experimental log-normal conductance histogram shape (normal distribution when conductance G is plotted in log scale) reported in single molecule-based molecular electronics (Figure 1b) (see Supplementary Note S1 in Supporting Information [SI] for a detailed history of conductance histograms in molecular electronics).[11,35−41]

Here, we explore $\pi-\pi$ intermolecular interaction energies from the electrochemical perspective (coupling between charge distributions) and molecular electronic perspective (coupling between orbitals) using a large array of ferrocene (Fc)-thiolated gold nanocrystals. First, we show that the two peaks observed in voltammograms on these systems can be controlled by the nanocrystal diameter. Each peak corresponds to a dense or dilute molecular organization structure located at the top or side facets of the nanocrystals, respectively. Second, the dense molecular organization structure is resolved by ultrahigh-vacuum scanning tunneling microscopy (UHV-STM). This structure is used as a reference for estimating t from quantum chemical calculations at the density functional theory (DFT) level. On the basis of current measurement statistics for ~3000 molecular junctions between the top of the nanocrystals and a conducting atomic force microscope (C-AFM) tip, we confirm the theoretical prediction that histograms shape is determined by cooperative effects.[21] Furthermore, we extend the previously proposed tight-binding formalism to fit the histograms.[21,34] The estimated electronic coupling energy distribution for t is quantitatively compared with quantum-chemical calculations. The φ and t obtained from CV traces and current histograms, respectively, are discussed on the basis of intermolecular distance fluctuations. Finally, we highlight the implications and perspectives of this study to molecular electronics, organic electronics, and electrochemistry.

Results. *Electrochemical Characterization of Fc-Thiolated Gold Nanocrystals.* We selected ferrocenylalkylthiol (FcC$_{11}$SH) as an archetype molecule with a π-conjugated head for electrochemistry[29,30,42,43] and molecular electronics.[12,14,29−46] CV is a powerful tool to gain insights into the molecular organization, extract surface coverage Γ, and evaluate the energy level of the HOMO ($E_{HOMO} \pm \delta E_{HOMO}$). In particular, as different molecular organization structures usually lead to multiple CV peaks,[47,48] the aim of this section is to demonstrate that molecules located at the top of the Fc-thiolated gold nanocrystals correspond to a single CV peak from which φ can be extracted.

Figure 2a−c (and Figures S1 and S2 in SI) show the experimental setup with NaClO$_4$ electrolyte (0.1 M) facing Fc molecules and the Au nanocrystal electrodes.[49] We have previously demonstrated the possibility of performing CV on Fc-thiolated gold nanocrystal surfaces,[14] although we studied only one dot diameter and did not investigated cooperative effects. CV cannot be performed at the single-dot level with these molecules because the currents are too weak ($\leq$fA range).[14,50,51]

First, we assess E_{HOMO} and dot-to-dot dispersion in E_{HOMO} (δE_{HOMO}) by CV. The voltammogram is averaged over millions
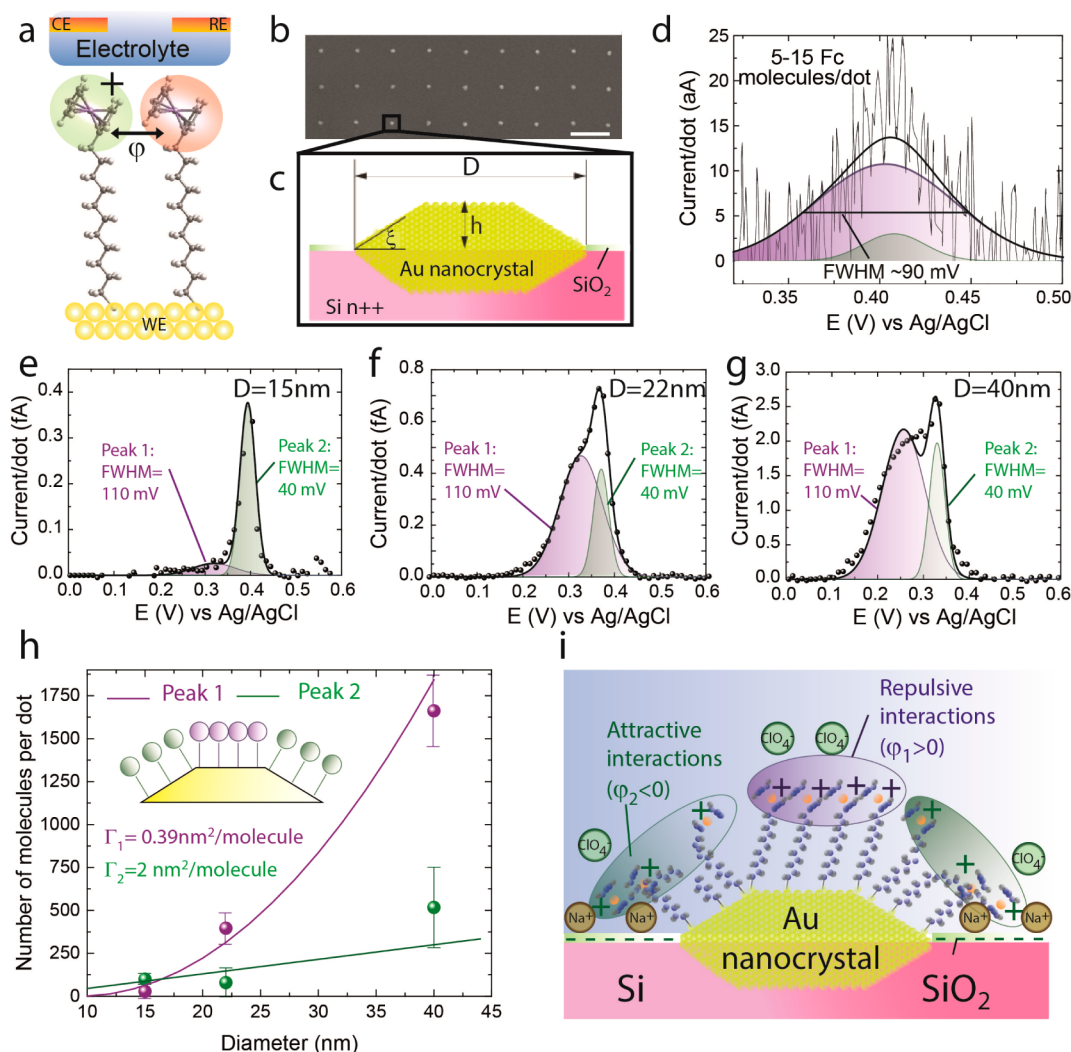
Figure 2. Quantitative analysis of molecular organization and intermolecular interaction energy φ from CV. (a) Schematic representation of intermolecular interaction in an electrochemical setup. Electrolyte is $NaClO_4$ (0.1 M). φ, Coulomb repulsion between adjacent molecules (see SI Methods); CE, counter electrode; RE, Ag/AgCl reference electrode; WE, working electrode (gold nanocrystals). (b) SEM image of gold nanocrystal array on highly doped silicon. Scale bar = 200 nm. (c) Schematic representation of a nanocrystal cross-section based on ref 49. Parameters of interest are the nanocrystal diameter D, height $h \approx 3$ nm and angle $\xi \approx 30°$. (d) Square wave voltammogram (SwV) for (1:10) $FcC_{11}SH$ SAM diluted with C_{12} molecules on an array of 15 nm diameter dots. Integration of the main peak area corresponds, after normalization (see SI Methods), to 5 to 15 $FcC_{11}SH$ molecules per dot. The curve is fitted with two peaks. The main peak has a fwhm ~90 mV ($\varphi \approx 0$). (e−g) CV results (oxidation peak) for arrays of $FcC_{11}SH$-coated gold nanoelectrodes of different diameters (as indicated). fwhm correspond to sweep rate of 1 V/s. Fitting parameters are indicated in Table S2. (h) Graphs showing number of molecules per dot (obtained from (e−g)) averaged with data from reduction peak (Figure S6). Error bars are based on dispersion between CV (oxidation/reduction peak and various speeds). Data are fitted with eq 3 (truncated cone approximation). Inset: Schematic representation of molecular organization. Peak 1 (purple) and peak 2 (green) correspond to molecules on top and sides, respectively. (i) Schematic representation of Fc-thiolated gold nanocrystals in $NaClO_4$ electrolyte when all Fc are oxidized.

of nanocrystals with a few Fc molecules per nanocrystal (diluted in a $C_{12}SH$ matrix) to avoid cooperative effects (Figure 2d). The peak energy position is in the expected range for Fc molecules (0.41 eV vs Ag/AgCl).[12,14,47,42] Furthermore, the voltammogram width at half-maximum (fwhm) is close to 90 mV for the main peak, that is, the theoretical value in the absence of interaction between redox moieties.[27] This result suggests that δE_{HOMO} is less than 45 meV (Figure S3).

Figure 2e−g shows conventional CV results for nanocrystals (of different diameters) that are fully covered with $FcC_{11}SH$ molecules (raw CV curves are shown in Figures S4−S6). Peak splitting can be observed.[42−44] The peak area is related to the total faradic charge and, therefore, to the number of molecules per dot. Only the number of molecules per nanocrystal related

to peak 1 significantly varies with nanocrystal diameter D (Figure 2h). On the basis of a simple model with a truncated conical shape for dots (Figure 2c), we suggest that peak 1 corresponds to molecules at the top of the dot, whereas peak 2 corresponds to molecules on the side of the dot (Figure 2h, inset). Thus, the density of molecules is smaller on the sides ($\Gamma \sim 2$ nm^2/molecule) than on the top ($\Gamma \sim 0.39$ nm^2/molecule) of the nanocrystals (see Figure 2h for fits and Methods for details). In other words, a highly ordered structure corresponding to a single peak in the voltammogram can be successfully formed on the top of the gold nanocrystals. This hypothesis is consistent with fwhm ≥90 mV for peak 1 (global repulsion between Fc moieties in the electrolytic media used[56]) and fwhm ≤90 mV for peak 2. The position and shape of the
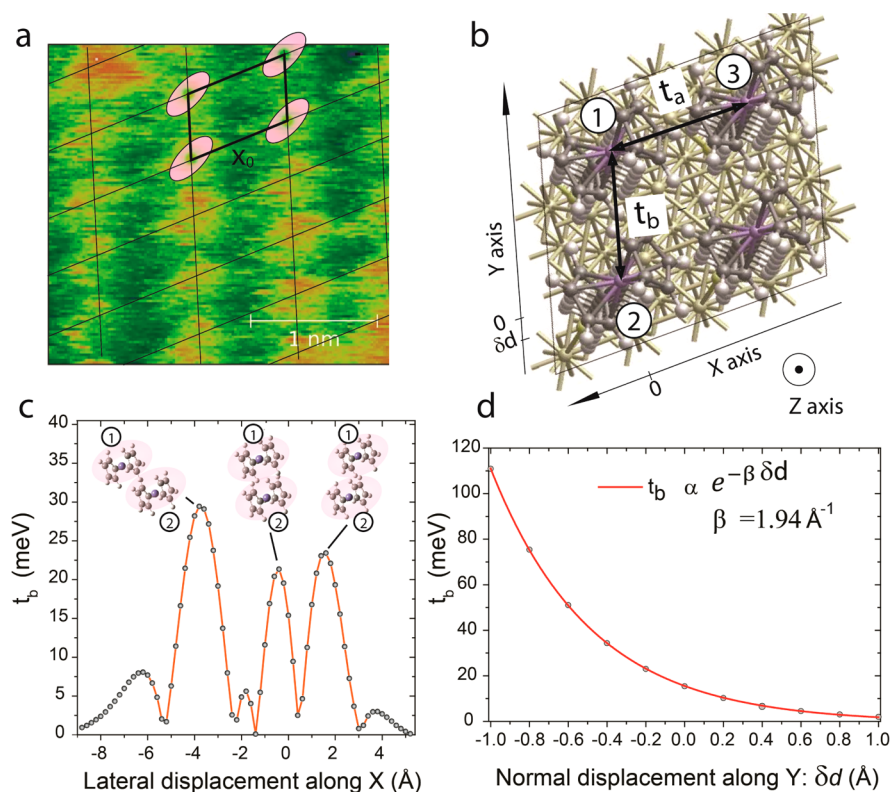
Figure 3. Estimation of cooperative effects from supramolecular organization and DFT calculations (a) UHV-STM image of a SAM of $FcC_{11}SH$ molecules grafted on gold. Molecular structure is resolved and used as reference for full DFT calculations. Periodic black lines with cell delimited by pink clouds indicate positions of Fc molecules. (b) Cell composed of four $FcC_{11}SH$ molecules based on (a,b). A number is attributed to each molecule due structural anisotropy. (φ_a, t_a) and (φ_b, t_b) refer to interactions between molecules 1 and 3 and molecules 1 and 2, respectively. X- and Y-axes are aligned along molecules 3 and 1 and molecules 2 and 1, respectively. (c) Full DFT calculation of parameter t_b between molecules 1 and 2. Position of molecule 2 is translated along the X-axis to mimic disorder. Inset: Molecular configuration at each maximum for t_b. (d) Evolution of t_b as a function of the variation of intermolecular separation δd modulated from the initial geometry (normal displacement = 0 Å). Decay ratios β_b is indicated.

second peak can be explained by a local change of the environment (presence of Na^+ counterions from negatively charged silica at the dot borders and pH > 2; Figure 2i) and a modification of ion-pairing equilibrium[47,52] (fewer ClO_4^- ions at dot borders due to SiO^- surface sites). CV on the smallest dots results in a single peak whose width is smaller than the width expected at room temperature without molecular interactions. This result could be technologically useful for improving the sensitivity of electrochemical biosensors beyond the thermal Nernst limit.[53−55]

The strength of electrostatic interactions for molecules located at the top of the gold nanocrystals can be quantitatively assessed by the extended Laviron model[27,56,57] (see Supplementary Methods). Coulomb interactions (φ when Fc moieties are fully oxidized) tune the fwhm's of the voltammograms because they are modulated by the fraction of oxidized species. Reasonable fits can be obtained with $\varphi = 4.5$ meV for all dot diameters (see Table S1 in SI for fit parameters). The φ obtained from CV will be linked to t from the current measurements in Discussion.

Estimation of t from Quantum-Chemical Calculations. The self-assembled monolayer (SAM) structure on a gold substrate has been resolved by UHV-STM (Figure 3a) and used as a reference for DFT calculations. The STM image shows a regular structure of elongated shapes corresponding to Fc groups. The extracted average area per molecule (0.40 nm²) is in agreement with our CV results and is slightly larger than

the 0.36 nm² considered for a hexagonal structure with a diameter of 0.66 nm per Fc.[58,59] The area corresponds to a configuration in which Fc units are at the same level in the vertical position. Each Fc unit forms a tilt angle of $56° \pm 15°$ with respect to the surface normal (Figure S7), consistent with estimates obtained by near-edge X-ray absorption fine structure spectroscopy $(60° \pm 5°)$[60] and by molecular dynamics simulations $(54° \pm 22°)$.[60]

When molecules are organized as in Figure 3b, t can be calculated by DFT for two neighboring Fc units (fragments). This simulation is only based on the Fc units and not on the full $FcC_{11}SH$ molecule because the contribution of the saturated part of the molecule to t is negligible. As structural fluctuations in monolayer organization are expected experimentally, we compute t_a and t_b between fragments of molecules 1 and 3 and molecules 1 and 2 at different positions along the X- and Y-axes. Figure 3c shows t_b when molecule 2 moves along the X-axis in a collinear geometry. t_b strongly depends on displacements of molecule 2 at the angstrom level because t is related to the electronic (rather than spatial) overlaps between π-orbitals.[61−64] Maxima are in the 20−30 meV range. Figure 3d shows the evolution of t_b as a function of the variation of the intermolecular distance d (δd) around the equilibrium position, without lateral displacement. The decay ratio $\beta_b = 1.94/$ Å is close to the tunnel decay ratio in molecular electronics. Similar results are obtained for t_a (cofacial geometry; see Figure S8). For consistency with our previous

studies, the B3LYP functional (see SI Methods) has been chosen due to the good agreement with mobility values extracted from the TRMC technique.[32] A recent theoretical study illustrated that B3LYP behaves very similarly to long-range corrected functionals and that the size of the basis set has a weak impact on the calculated transfer integrals.[65]

Overall, the results indicate the presence of electronic coupling between the π-conjugated Fc molecules and suggest that a signature of cooperative effects should be observed on current measurements.

Cooperative Effects on Current Histograms. We have conducted the statistical study proposed in ref 21 (i.e., current histograms). "Nano-SAMs" (i.e., SAMs with diameters of a few tens of nanometers) are ideal for this experiment. Use of nano-SAMs enables us to obtain sufficient molecules for cooperative effects but limits the number of molecules to avoid averaging over many molecular structures, grain boundaries, and defects. The C-AFM, as the top electrode,[66] is swept over thousands of nanocrystals.[39] We previously showed that log-normal histograms are systematically obtained when such a statistical study is performed with nano-SAMs composed of alkyl chains without π-groups.[39] In contrast, as predicted in ref 21, we find that the presence of cooperativity between π-conjugated orbitals (in the headgroup) affects the line shape of histograms. Figure 4a is the current histogram obtained on FcC$_{11}$SH nano-SAMs at -0.6 V for 45 nm diameter gold nanocrystals (2D histogram corresponding to different tip biases is shown in Figures S9). The related histogram line shape can be nicely fitted with asymmetric double sigmoidal function when the current histograms are plotted in log scale (see Methods and Table S2 for fitting parameters). In the case of 15 nm diameter nanocrystals, a second peak, corresponding to another molecular organization structure,[39] appears at a lower current in the histograms (Figure 4b). We suggest that this peak, which is barely seen in the histogram Figure 4a, is averaged on larger dots. Fitting parameters for the main current peak are almost unchanged (see Table S2). When FcC$_{11}$ molecules are diluted 1:1 with dodecanethiol molecules (C$_{12}$SH) to reduce coupling between π molecules, the log-normal histogram is recovered (Figure 4c), similarly to alkyl-chain-coated nanocrystals.[39]

We tried to fit the current histograms using a coherent scattering formalism, similar to the one proposed in ref 21, with the additional consideration of asymmetrical coupling to the electrodes and the possibility of simulating up to 9 × 9 molecules (only two molecules were considered in ref 21). Figure 5a illustrates the modeled system. Each Fc molecule is considered as a single-level quantum dot coupled to both electrodes. Dots are coupled together with coupling term t in a tight binding model. This coupling term is equivalent to the transfer integral in DFT. For simplicity, t is considered to be identical along both axes in the plane. Each molecule within a molecular junction composed of $N \times N$ molecules has the same parameters ε (molecule orbital energy), V_t, V_b, (molecules coupling to top and bottom electrodes, respectively), and t. Cooperative effects, whose strength is controlled by parameters V_t, V_b, t, and N, cause a smearing out of the energy-dependent transmission coefficient with a peak transmission being less than one[21] (see Figures S13−S15 in SI for additional illustrations). The current, obtained from the integral of the transmission coefficient over a range of energy set by the external potential, depends on these parameters accordingly (see SI Methods). To generate current histograms, V_t, V_b, t, and ε are chosen from Gaussian distributions with predefined
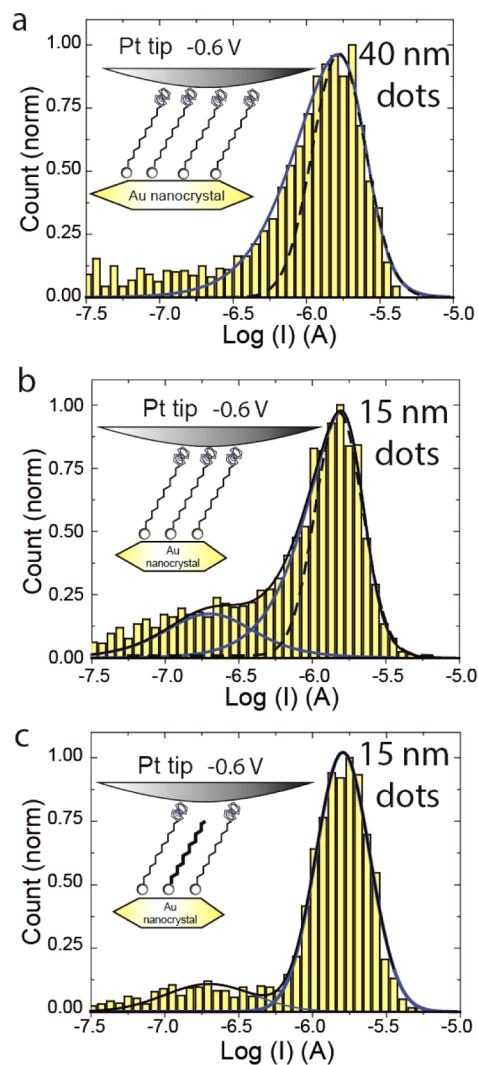

Figure 4. Current histograms used to evaluate $\pi-\pi$ intermolecular interaction energy ($\sim$3000 counts per histogram). Current histogram obtained at a tip voltage of -0.6 V for (a) 40 and (b) 15 nm diameter dots (with 5 nm diameter on top). Plain curve is the fit with asymmetric double sigmoidal function (eq 4). Dashed curve is the log-normal fit. Inset: Schematic view of the setup. (c) Same as (b) but with a (1:1) FcC$_{11}$SH/C$_{12}$SH-diluted SAM. Fitting parameters are shown in Table S2.

means and SDs (e.g., eq 1a) for each individual molecular junction. For t, we additionally considered eq 1b to explicitly consider the fluctuation of the intermolecular distance (see Figure 3d)

$$t = \langle t \rangle + \delta t \qquad (1a)$$

$$t = t_0 \exp(-\beta \delta d) \qquad (1b)$$

where δd in eq 1b is chosen from a Gaussian distribution. A step-by-step fitting protocol is detailed in Methods and Figures S10 and S11 in SI. Figure 5b illustrates the possibility of generating histograms that reproduce the experiments. Optimized parameters for 9 × 9 molecules using eq 1a for t ($t = 0.04$ eV, $V_t = 0.401$ eV, $V_b = 0.144$ eV, $\delta\varepsilon = 40$ meV, $\delta t = 0.14$ eV, and $\delta V = 22$ meV) are in the range of those considered in ref 21 based on ref 67 where t was 0.1 eV, $V_t = V_b = 0.6$ eV, $\delta t = 75$ meV, $\delta V = 37$ meV, and $\delta\varepsilon = 30$ meV). Considering eq 1b for t gives an even better fit to experimental data with $t_0 =$
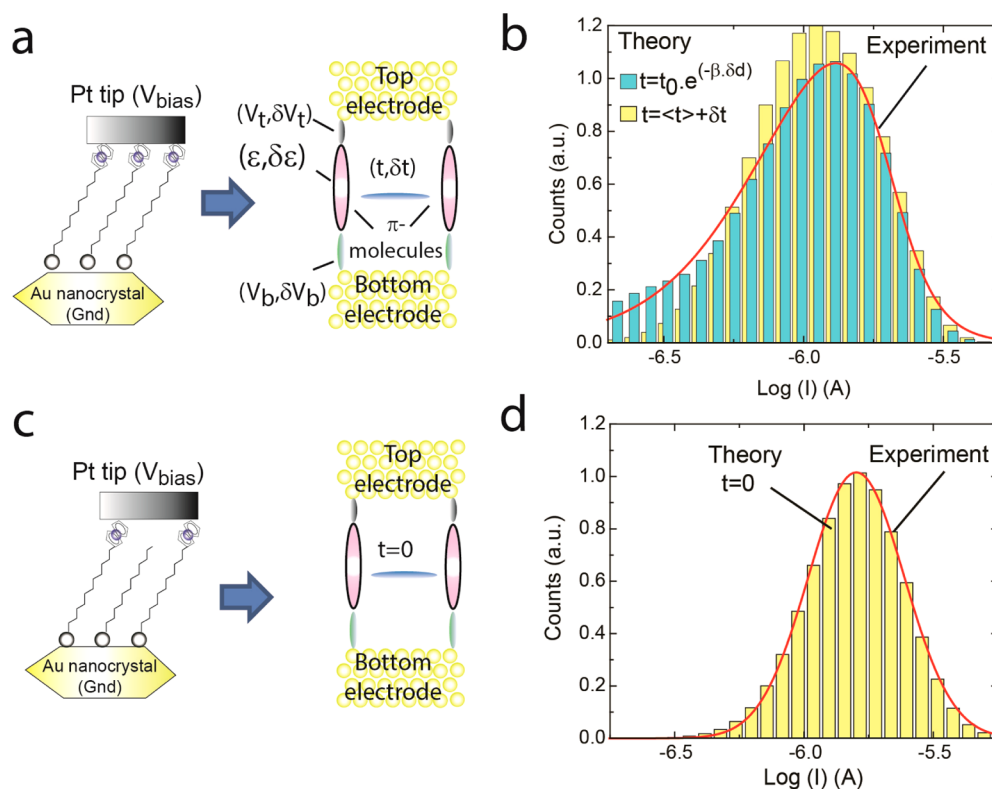
Figure 5. Histograms fits with Landauer Buttiker Imry formalism. (a) Schematic representation of the model. Each molecule (quantum dot) is coupled to other molecules with coupling term t and coupled to top/bottom electrodes with coupling energies V_t and V_b, respectively. ε, molecule orbital energy. SDs of these parameters are used to generate histograms. Related experimental setup shown for clarity. (b) Experimental (V_{tip} = −0.6 V) and simulated histograms (V_t = 0.401 eV, V_b = 0.144 eV, δV = 22 meV, ε = 0.2 eV, t = 0.04 eV, δt = 140 meV, t_0 = 0.34 eV, β = 1.96/Å, SD(δd) = 0.8 Å) considering 81 molecules. (c) Schematic representation of model with fewer molecular interactions. Parameters are same as in (a) except t = 0. Related experimental setup (diluted monolayer) is shown for clarity. (d) Experimental (V_{tip} = −0.6 V) and simulated histograms (t = 0).

0.34 eV, β = 1.96/Å, and SD(δd) = 0.8 Å. When intermolecular coupling is suppressed (t = 0) while keeping other parameters constant to mimic the diluted monolayer (Figure 5c), the resulting log-normal histogram reproduces the experimental results (Figure 5d).

Discussion. In molecular or organic electronics, comparisons of experimental and theoretical charge transport data are usually qualitative. Therefore, any step toward a more quantitative analysis is important to the field.

A strong coupling asymmetry of $\alpha = V_t^2/(V_t^2 + V_b^2) \approx 0.9$ was required to fit histograms (see Figure S10 in SI), as expected from the structure of the molecule and previous studies.[12,14] The "large" values of V_t and V_b (molecular orbital energy broadening amounts of 100 and 15 meV, respectively) confirm our expectation of strong molecule/electrode couplings, which we previously exploited to obtain a high-frequency molecular diode.[14]

Extracted distributions of t corresponding to best fits in Figure 5d are shown in Figure 6a. We have explored two t distributions corresponding to eqs 1a and 1b. In both cases, maxima are found at $t \approx 35$ meV, which is in the expected range from our DFT calculations. However, both deviate quantitatively from the theoretical distribution prediction for t based on thermal molecular motions (SD(t) $\approx$ ⟨t⟩ in eq 1a).[25] Using eq 1a, we find SD(t) $\approx$ 140 meV, suggesting that the structural fluctuations are larger than those generated from solely thermal motions (phonons). Structural fluctuations are explicitly considered with parameter δd in eq 1b. The extracted SD(δd) = 0.8 Å is reasonable given that a more packed configuration for

these monolayers is possible.[12] On the basis of these results, we suggest that van der Waals interactions between alkyl chains, which compete with the $\pi-\pi$ interactions in the molecular organization of such monolayers,[12] could play a role in the distribution of t.

We stress that the number of molecules $N \times N$ considered for current histograms generation affects the quantitative extraction of t. Approximately 150 molecules are used in the experiment. A large enough N was required in the model to avoid overestimating the extracted value of t (Figure S11 in SI). At $N = 9$, the extracted t depends to a lesser extent on the molecule/electrode coupling parameters, which reduces the error on the estimated t (Figure S11 in SI). We suggest that $t \approx 35 \pm 20$ meV is extracted from the present model based on both t distributions and the possible error on V_t and V_b.

From this quantitative analysis on t, we can discuss the results in the general contexts of charge transport in organic semiconductors[32,33,68] and chemical characterization tools.

As high-mobility organic semiconductors are often composed of a π-conjugated backbone substituted by one or more alkyl side chains,[32] as in the present study, a t distribution following eq 1b may be considered in charge transport models. Semiclassical theories of charge transport in organic semiconductors show that the electron transfer (hopping) rates along the π-conjugated molecular planes scale as t^2. Figure 6b represents such probability distributions for t^2 corresponding to the two t distributions shown in Figure 6a (related to eq 1a and 1b). Distributions have similar shapes in both cases, but the tail is narrower for the Gaussian distribution of t. In both cases, the
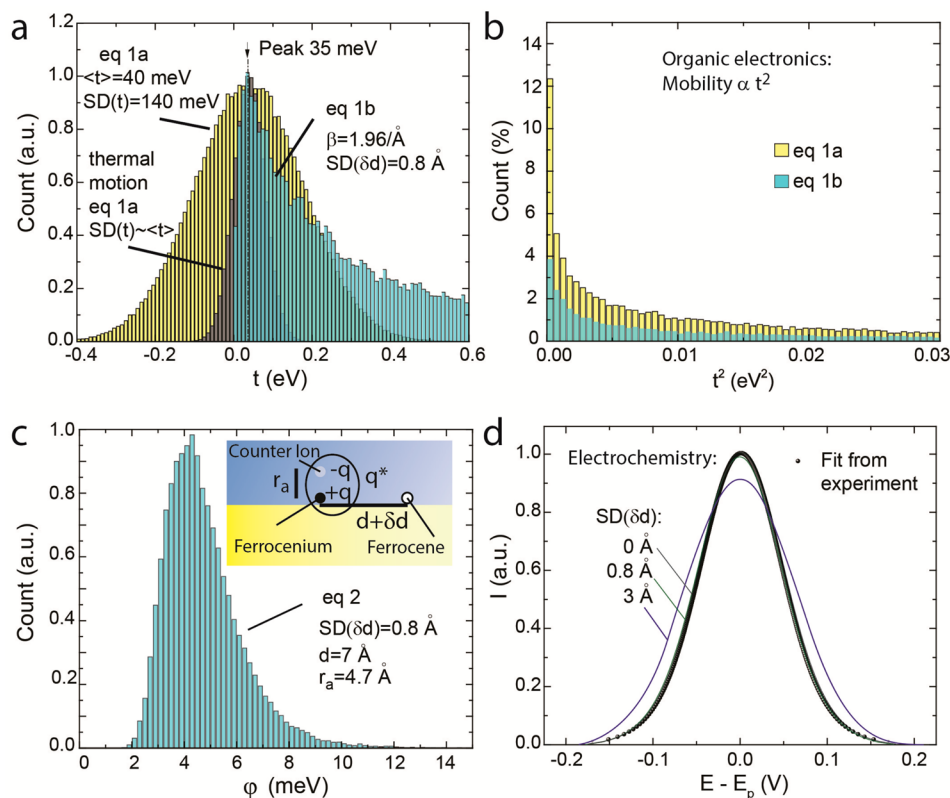
Figure 6. Extracted distributions of t and implications for organic electronic and electrochemical field. (a) Distribution of t obtained from best fits in Figure 5d with eqs 1a and 1b. Expected (Gaussian) distribution from solely thermal motions shown in gray. Each electronic level has an associated t that can be positive or negative, so the sign is of little importance. (b) t^2 distribution obtained from (a). (c) Estimated distribution of φ from eq 2 given an intermolecular distance fluctuation of $\delta d = 0.8$ Å. Inset: Schematic representation of the electrostatic model (eq 2). (d) Experimental and theoretical CV results (coupled eq 2 and eq S1) with $\delta d = 0$, 0.8, and 3 Å. Energy level of Fc versus Ag/AgCl (E_p) is used to center the CV peak at 0.

broadened distribution of t^2 would open new hopping pathways.

The exploration of $\pi-\pi$ intermolecular interaction energies from both CV and current histograms using the same samples composed of a large array of Fc-thiolated gold nanocrystals enables a direct comparison of both techniques as chemical characterization tools. Parameters φ and t are different in nature, but both are related to the molecular organization. As for t with eq 1b, φ can be related to δd from a simple electrostatic model (Figure 6c, inset):

$$\varphi = q \frac{1 - \left(1 + \left(\frac{r_a}{(d + \delta d)}\right)^2\right)^{-0.5}}{4\pi\varepsilon_0\varepsilon_r(d + \delta d)} \quad (2)$$

r_a is the counterion pairing distance, q is the elementary charge, ε_0 and ε_r are the dielectric permittivity of vacuum and the relative permittivity of water, respectively. For $d = 7$ Å and $\delta d = 0$ Å, $\varphi = 4.5$ meV obtained from fits of the first peak in Figure 2e−g corresponds to an Fc-ClO$_4^-$ ion pairing distance of 4.9 Å (5.5 Å is expected from molecular dynamics simulations[69]). With eq 2, a Gaussian distribution for δd implies a non-Gaussian distribution for φ (Figure 6c). Combining eq 2 and the extended Laviron model (see SI Methods), we see that such a distribution should induce a broadening of the CV peak, but only when $d + \delta d$ approaches the ion-pairing distance (Figure 6d). Therefore, CV would not be sufficiently sensitive to assess information on the small molecular organization fluctuations expected here (e.g., SD(δd) = 0.8 Å from parameter t analysis).

This feature illustrates the potential of using t as an ultrasensitive chemical characterization parameter.

In summary, we have investigated the possibility of assessing the $\pi-\pi$ electronic couplings from charge transport measurements in a connected device, using a statistical analysis of current from a large array of Fc-thiolated gold nanocrystals. The results have been quantitatively compared to DFT calculations. Extracted parameters, including a molecule/electrode coupling asymmetry α of 0.9 and t of 35 meV, were in the range of expectations. However, the distribution of t was broader than expected from the solely thermal fluctuations. This observation is attributed to structural fluctuations and to a variation of the intermolecular distance of 0.8 Å in the model. The results confirm the need for charge transport model to consider small structural fluctuations, even on the order of 1 Å; however, CV does not have sufficient sensitivity to reveal such small fluctuations. This limitation may be overcome by measuring extremely small CV currents (on the single-dot level), and performing statistical analyses on φ (as predicted in Figure 6c). The origin of these structural fluctuations remains unclear, but could be related to the competitive $\pi-\pi$ and $\sigma-\sigma$ interactions due to the presence of alkyl chains. Overall, the present study provides insights into understanding $\pi-\pi$ intermolecular interactions in organic and (bio-) molecular devices. The findings confirm that Landauer-type coherent-scattering models, which are usually dedicated to low-temperature mesoscopic physics, are relevant at room temperature for molecular electronics, even in the presence of cooperative effects. Statistical current analysis could be applied

to various systems, because current histograms represent a common approach in molecular junctions. The study of $\pi-\pi$ electronic couplings is a unique opportunity to link quantum chemistry, mesoscopic physics, organic electronics, and electrochemistry, indicating the importance of each subfield in the development of organic electronics.

Methods. Additional methodological information related to STM,[59,70] gold nanodot fabrication,[49,71] monolayer self-assembly, experimental conditions for CV and related fits, image treatment DFT calculations and theoretical histogram generation is available in the SI Methods.

UHV STM. The high-resolution image was performed at room temperature with a substrate biased at 2 V and at a constant current of 1 pA.

Areas of Top and Side Facets of the Nanocrystals. To estimate the number of molecules per peak, the area was considered from the following formula, based on Figure 2c

$$\frac{\pi}{4}\left(\frac{D-2h}{\tan\xi}\right)^2 + \pi\left(\frac{D-2h}{\tan\xi}\right)\frac{h}{\sin\xi} \tag{3}$$

where the first term corresponds to the area on the top and the second term to the area on the sides of the nanocrystal. Reasonable fits are obtained with $h = 2.7$ nm and $\xi = 30°$, as expected from the nanocrystal structure.

C-AFM. We measured current voltage by using C-AFM (Dimension 3100, Veeco) with a PtIr-coated tip on molecules[14,66,72] in N_2 atmosphere. Each count in the statistical analysis corresponds to a single and independent gold nanodot. The tip curvature radius is about 40 nm (estimated by SEM), and the force constant is in the range of 0.17–0.2 N/m. C-AFM measurements were taken at loading forces of 15 and 30 nN for the smallest and largest dots, respectively to keep a similar force per surface unit. As shown in ref 14, a weak effect of the force is observed for these molecules in the range of 10–30 nN. In scanning mode, the bias is fixed and the tip sweep frequency is set at 0.5 Hz. With our experimental setup being limited to 512 pixels/image, the parameters lead to a typical number of 3000 counts for a $6 \times 6 \ \mu$m C-AFM image. In the presence of $\pi-\pi$ electronic couplings, current histogram peaks are well-fitted with an asymmetric double sigmoidal function $f(x)$ given by

$$f(x) = y_0 + A\frac{1}{1 + e^{-(x-x_c+w_1/2)/w_2}}\left(1 - \frac{1}{1 + e^{-(x-x_c-w_1/2)/w_3}}\right) \tag{4}$$

where the values of the various parameters are presented in SI Table 2.

Landauer Imry Buttiker Formalism and Histograms Fits. The model has been adapted from ref 21 to account for a large number of molecules and asymmetrical contacts (detail in SI Methods). It provides a good description of the fundamental aspects of electron transport via the computation of the energy-dependent transmission through the device. The formalism described in ref 21 focused on the zero-bias conductance (and at low temperature), a result that can be extended to the evaluation of the current at low bias, provided that one integrates the transmission over a range of energy given by the external potential. Here we have used this model with conditions of relatively high bias and at room temperature. The assumption that the Landauer approach remains applicable under such conditions is often made in the field of molecular electronics with a single-level model.[31] We believe that these assumptions are further justified due to the strong coupling of

the Fc molecules, as evidenced by the level broadening estimated in the range of 100 meV. The generation of current histograms (instead of conductance histograms in ref 21) required an additional assumption (midpoint rule) to efficiently compute the 10^6 realizations (see SI Methods). The validity of this approximation has been confirmed for the present study (Figure S14 in SI).

The process of fitting the line shape of the experimental histograms relies on a relatively large number of variables, which can be defined by a step by step procedure. We considered a site energy $\varepsilon = 0.2$ eV versus Fermi level at $V_{bias} = 0$ V, given the CV results and related energy band diagram proposed in ref 14. An upper limit of $\delta\varepsilon < 45$ meV was considered based on CV analysis (Figure S 3d). First, we optimized the parameters for 3×3 molecules due to computational time. Because $\delta\varepsilon$ does not significantly affect the extracted value of t (Figure S10), we considered $\delta\varepsilon = 40$ meV (similar to the value considered in ref 21. V_t and V_b were adjusted to get a good current level and to reproduce the histogram shape. An optimal asymmetry factor of $\alpha = 0.9$ was considered (Figure S10), which is in agreement with refs 12 and 14. δV was tuned to fit the histogram line shape when $t = 0$ (mixed monolayer). δt was tuned with t while fitting asymmetric histograms line shapes. Current histograms were generated based on 10^6 realizations. When the number of molecules in the matrix is large (e.g., 9×9 molecules), histogram fitting takes several days. Therefore, statistical studies on larger organic crystal systems[73] would require optimization of computation time. Efficient hardwares (i.e., Ising machine) is being developed to solve such problems efficiently.[74,75]

■ ASSOCIATED CONTENT

Ⓢ Supporting Information

The Supporting Information is available free of charge on the ACS Publications website at DOI: 10.1021/acs.nanolett.7b00804.

Additional information, figures, tables, and methods (PDF)

■ AUTHOR INFORMATION

Corresponding Author

*E-mail: nicolas.clement@lab.ntt.co.jp.

ORCID Ⓘ

D. Vuillaume: 0000-0002-3362-1669

N. Clément: 0000-0002-4924-4087

Present Address

(J.T.) Department of Chemistry, NUS 3 Science Drive 3 Singapore 117543.

Author Contributions

[#]J.T. and J.R. contributed equally to the work.

Notes

The authors declare no competing financial interest.

■ ACKNOWLEDGMENTS

■ REFERENCES

(1) Hunter, C. A.; Sanders, J. K. M. *J. Am. Chem. Soc.* **1990**, *112*, 5525−5534.

(2) Hermann, J.; Alfe, D.; Tkatchenko, A. *Nat. Commun.* **2017**, *8*, 14052.

(3) Mignon, P.; Loverix, S.; Steyaert, J.; Geerlings, P. *Nucl. Acid. Res.* **2005**, *33*, 1779−1789.

(4) Zhang, S. *Nat. Biotechnol.* **2003**, *21*, 1171−1178.

(5) Meyer, E. A.; Castellano, R. K.; Diederich, F. *Angew. Chem., Int. Ed.* **2003**, *42*, 1210−1250.

(6) Krishnamurthy, V. M.; Kaufman, G. K.; Urbach, A. R.; Gitlin, I.; Gudiksen, K. L.; Weibel, D. B.; Whitesides, G. M. *Chem. Rev.* **2008**, *108*, 946−1051.

(7) Moulton, B.; Zaworotko, M. J. *Chem. Rev.* **2001**, *101*, 1629−1658.

(8) Cornil, J.; Beljonne, D.; Calbert, J. P.; Bredas, J. L. *Adv. Mater.* **2001**, *13*, 1053−1067.

(9) Kamtekar, K. T.; Monkman, A. P.; Bryce, M. R. *Adv. Mater.* **2010**, *22*, 572−582.

(10) Yi, H. T.; Payne, M. M.; Anthony, J. E.; Podzorov, V. *Nat. Commun.* **2012**, *3*, 1259.

(11) Wu, S. M.; González, M. T.; Huber, R.; Grunder, S.; Mayor, M.; Schönenberger, C.; Calame, M. *Nat. Nanotechnol.* **2008**, *3*, 569−574.

(12) Nerngchamnong, N.; Yuan, L.; Qi, D. C.; Li, J.; Thompson, D.; Nijhuis, C. A. *Nat. Nanotechnol.* **2013**, *8*, 113−118.

(13) Venkataraman, L.; Klare, J. E.; Nuckolls, C.; Hybertsen, M. S.; Steigerwald, M. L. *Nature* **2006**, *442*, 904−907.

(14) Trasobares, J.; Vuillaume, D.; Théron, D.; Clément, N. *Nat. Commun.* **2016**, *7*, 12850−12856.

(15) Cheng, Z. L.; Skouta, R.; Vazquez, H.; Widawsky, J. R.; Schneebeli, S.; Chen, W.; Hybertsen, M. S.; Breslow, R.; Venkataraman, L. *Nat. Nanotechnol.* **2011**, *6*, 353−357.

(16) Renaud, N.; Harris, M. A.; Singh, A. P. N.; Berlin, Y. A.; Ratner, M. A.; Wasielewski, M. R.; Lewis, F. D.; Grozema, F. C. *Nat. Chem.* **2016**, *8*, 1015−1021.

(17) Marcus, R. A. *Rev. Mod. Phys.* **1993**, *65*, 599−610.

(18) Crispin, X.; Cornil, J.; Friedlein, R.; Okudaira, K. K.; Lemaur, V.; Crispin, A.; Kestemont, G.; Lehmann, M.; Fahlman, M.; Lazzaroni, R.; Geerts, Y.; Wendin, G.; Ueno, N.; Brédas, J. L.; Salaneck, W. L. *J. Am. Chem. Soc.* **2004**, *126*, 11889−11899.

(19) Ciliberto, E.; Doris, K. A.; Pietro, W. J.; Reisner, G. M.; Ellis, D. E.; Fragala, I.; Herbstein, F. H.; Ratner, M. A.; Marks, T. J. *J. Am. Chem. Soc.* **1984**, *106*, 7748−7761.

(20) Hutchison, G. R.; Ratner, M. A.; Marks, T. J. *J. Am. Chem. Soc.* **2005**, *127*, 16866−1688.

(21) Reuter, M. G.; Hersam, M. C.; Seideman, T.; Ratner, M. A. *Nano Lett.* **2012**, *12*, 2243−2248.

(22) Reuter, M. G.; Seideman, T.; Ratner, M. A. *Nano Lett.* **2011**, *11*, 4693−4696.

(23) Troisi, A.; Orlandi, G. *Phys. Rev. Lett.* **2006**, *96*, 086601−086604.

(24) Troisi, A.; Orlandi, G. *J. Phys. Chem. A* **2006**, *110*, 4065−4070.

(25) Martinelli, N. G.; Olivier, Y.; Athanasopoulos, S.; Ruiz Delgado, M.-C.; Pigg, K. R.; da Silva Filho, D. A.; Sanchez-Carrera, R. S.; Venuti, E.; Della Valle, R. G.; Bredas, J.-L.; Beljonne, D.; Cornil, J. *ChemPhysChem* **2009**, *10*, 2265−2273.

(26) Albery, W. J.; Boutelle, M. G.; Colby, P. J.; Hillman, A. R. *J. Electroanal. Chem. Interfacial Electrochem.* **1982**, *133*, 135−145.

(27) Laviron, E. *J. Electroanal. Chem. Interfacial Electrochem.* **1979**, *100*, 263−275.

(28) Temkin, M. I. *Zh. Fiz. Khim.* **1941**, *15*, 296−303.

(29) Wierzbinski, E.; Venkatramani, R.; Davis, K. L.; Bezer, S.; Kong, J.; Xing, Y.; Borguet, E.; Achim, C.; Beratan, D. N.; Waldeck, D. H. *ACS Nano* **2013**, *7*, 5391−5401.

(30) Hossain, M. S.; Bevan, K. H. *J. Phys. Chem. C* **2016**, *120*, 188−194.

(31) Garrigues, A. R.; Yuan, L.; Wang, L.; Mucciolo, E. R.; Thomson, D.; del Barco, E.; Nijhuis, C. A. *Sci. Rep.* **2016**, *6*, 26517−26523.

(32) Tsutsui, Y.; Schweicher, G.; Chattopadhyay, B.; Sakurai, T.; Arlin, J.-B.; Ruzie, C.; Aliev, A.; Ciesielski, A.; Colella, S.; Kennedy, A. R.; Lemaur, V.; Olivier, Y.; Hadji, R.; Sanguinet, L.; Castet, F.; Osella, S.; Dudenko, D.; Beljonne, D.; Cornil, J.; Samori, P.; Seki, S.; Geerts, Y. H. *Adv. Mater.* **2016**, *28*, 7106−7114.

(33) Coropceanu, V.; Cornil, J.; da Silva Filho, D. A.; Olivier, Y.; Silbey, R.; Brédas, J. L. *Chem. Rev.* **2007**, *107*, 926−952.

(34) Reuter, M. G. *J. Chem. Phys.* **2010**, *133*, 034703−034708.

(35) Li, C.; Pobelov, I.; Wandlowski, T.; Bagrets, A.; Arnold, A.; Evers, F. *J. Am. Chem. Soc.* **2008**, *130*, 318−326.

(36) Engelkes, V. B.; Beebe, J. M.; Frisbie, C. D. *J. Phys. Chem. B* **2005**, *109*, 16801−16810.

(37) Gonzalez, M. T.; Wu, S.; Huber, R.; van der Molen, S. J.; Schönenberger, C.; Calame, M. *Nano Lett.* **2006**, *6*, 2238−2242.

(38) Guo, S.; Hihath, J.; Diez-Perez, I.; Tao, N. *J. Am. Chem. Soc.* **2011**, *133*, 19189−19197.

(39) Smaali, K.; Clément, N.; Patriarche, G.; Vuillaume, D. *ACS Nano* **2012**, *6*, 4639−4647.

(40) Lörtscher, E.; Weber, H. B.; Riel, H. *Phys. Rev. Lett.* **2007**, *98*, 176807−17810.

(41) Andrews, D. Q.; van Duyne, R. P.; Ratner, M. A. *Nano Lett.* **2008**, *8*, 1120−1126.

(42) Lee, L. Y.; Sutherland, T. C.; Rucareanu, S.; Lennox, R. B. *Langmuir* **2006**, *22*, 4438−4444.

(43) Valincius, G.; Niaura, G.; Kazakevieiene, B.; Talaikyte, Z.; Kazemekaite, M.; Butkus, E.; Razumas, V. *Langmuir* **2004**, *20*, 6631−6638.

(44) Nijhuis, C. A.; Reus, W. F.; Whitesides, G. M. *J. Am. Chem. Soc.* **2009**, *131*, 17814−17827.

(45) Nijhuis, C. A.; Reus, W. F.; Barber, J. R.; Dickey, M. D.; Whitesides, G. M. *Nano Lett.* **2010**, *10*, 3611−3619.

(46) Jeong, H.; et al. *Adv. Funct. Mater.* **2014**, *24*, 2472−2480.

(47) Tian, H.; Dai, Y.; Shao, H.; Yu, H. Z. *J. Phys. Chem. C* **2013**, *117*, 1006−1012.

(48) Nerngchamnong, N.; Thompson, D.; Cao, L.; Yuan, L.; Jiang, L.; Roemer, M.; Nijhuis, C. A. *J. Phys. Chem. C* **2015**, *119*, 21978−21991.

(49) Clement, N.; Patriarche, G.; Smaali, K.; Vaurette, F.; Nishiguchi, K.; Troadec, D.; Fujiwara, A.; Vuillaume, D. *Small* **2011**, *7*, 2607−2613.

(50) Anne, A.; Cambril, E.; Chovin, A.; Demaille, C.; Goyer, C. *ACS Nano* **2009**, *3*, 2927−2940.

(51) Huang, K.; Anne, A.; Bahri, M. A.; Demaille, C. *ACS Nano* **2013**, *7*, 4151−4163.

(52) Uosaki, K.; Sato, Y.; Kita, H. *Langmuir* **1991**, *7*, 1510−1514.

(53) Yagati, K.; Jung, M.; Kim, S.-U.; Min, J.; Choi, J. W. *Thin Solid Films* **2009**, *518*, 634−637.

(54) Huang, K.; Anne, A.; Bahri, A.; Demaille, C. *ACS Nano* **2013**, *7*, 4151−4163.

(55) Nault, L.; Taofifenua, C.; Anne, A.; Chovin, A.; Demaille, C.; Besong-Ndika, J.; Cardinale, D.; Carette, N.; Michon, T.; Walter, J. *ACS Nano* **2015**, *9*, 4911−4924.

(56) Alévêque, O.; Blanchard, P. Y.; Gautier, C.; Dias, M.; Breton, T.; Levillain, E. *Electrochem. Commun.* **2010**, *12*, 1462−1466.

(57) Alévêque, O.; Levillain, E. *Electrochem. Commun.* **2013**, *34*, 165−169.

(58) Chidsey, C. E. D.; Bertozzi, C. R.; Putvinski, T. M.; Mujsce, A. M. *J. Am. Chem. Soc.* **1990**, *112*, 4301−4306.

(59) Muller-Meskamp, L.; Lüssem, B.; Karthäuser, S.; Prikhodovski, S.; Homberger, M.; Simon, U.; Waser, R. *Phys. Status Solidi A* **2006**, *203*, 1448−1452.

(60) Yuan, L.; Nerngchamnong, N.; Cao, L.; Hamoudi, H.; del Barco, E.; Roemer, M.; Sriramula, R. K.; Thomson, D.; Nijhuis, C. A. *Nat. Commun.* **2015**, *6*, 6324−6331.

(61) Viani, L.; Olivier, Y.; Athanasopoulos, S.; da Silva Filho, D. A.; Hulliger, J.; Bredas, J. L.; Gierschner, J.; Cornil, J. *ChemPhysChem* **2010**, *11*, 1062−1068.

(62) Feng, X.; Marcon, V.; Pisula, W.; Hansen, M. R.; Kirkpatrick, J.; Grozema, F.; Andrienko, D.; Kremer, K.; Mullen, K. *Nat. Mater.* **2009**, *8*, 421−436.

(63) Bredas, J. L.; Calbert, J. P.; da Silva, D. A.; Cornil, J. *Proc. Natl. Acad. Sci. U. S. A.* **2002**, *99*, 5804−5809.

(64) Valeev, E. F.; Coropceanu, V.; da Silva Filho, D. A.; Salman, S.; Brédas, J. L. *J. Am. Chem. Soc.* **2006**, *128*, 9882−9886.

(65) Mikolajczyk, M. M.; Zalesny, R.; Czyznikowska, Z.; Toman, P.; Leszczynski, J. B, 28, 7106-W. *J. Mol. Model.* **2011**, *17*, 2143−2149.

(66) Wold, D. J.; Frisbie, C. D. *J. Am. Chem. Soc.* **2000**, *122*, 2970−2971.

(67) Landau, A.; Kronik, L.; Nitzan, A. *J. Comput. Theor. Nanosci.* **2008**, *5*, 535−545.

(68) Uratani, H.; Kubo, S.; Shizu, K.; Suzuki, F.; Fukushima, T.; Kaji, H. *Sci. Rep.* **2016**, *6*, 39128−39124.

(69) Filippini, G.; Goujon, F.; Bonal, C.; Malfreyt, P. *J. Phys. Chem. B* **2010**, *114*, 12897−12907.

(70) Nerngchamnong, N.; Wu, H.; Sotthewes, K.; Yuan, L.; Cao, L.; Roemer, M.; Lu, J.; Loh, K. P.; Troadec, C.; Zandvliet, H. J. W.; Nijhuis, C. A. *Langmuir* **2014**, *30*, 13447−13455.

(71) Trasobares, J.; Vaurette, F.; Francois, M.; Romijn, H.; Codron, J.-L.; Vuillaume, D.; Theron, D.; Clement, N. *Beilstein J. Nanotechnol.* **2014**, *5*, 1918−1925.

(72) Smaali, K.; Desbief, S.; Foti, G.; Frederiksen, T.; Sanchez-Portal, D.; Arnau, A.; Nys, J.-P.; Leclere, P.; Vuillaume, D.; Clement, N. *Nanoscale* **2015**, *7*, 1809−1819.

(73) Hasegawa, Y.; Yamada, Y.; Hosokai, T.; Koswattage, K. R.; Yano, M.; Wakayama, Y.; Sasaki, M. *J. Phys. Chem. C* **2016**, *120*, 21536−21542.

(74) Inagaki, T.; Inaba, K.; Hamerly, R.; Inoue, K.; Yamamoto, Y.; Takesue, H. *Nat. Photonics* **2016**, *10*, 415−419.

(75) Mahboob, I.; Okamoto, H.; Yamaguchi, H. *Sci.Adv.* **2016**, *2*, 1600236−1600241.